catalysts

MDPI

Article

Comparing the Efficiency of N-Doped TiO_2 and N-Doped Bi_2MoO_6 Photo Catalysts for MB and Lignin Photodegradation

Ricardo Rangel [1,*], Verónica Janneth Cedeño [1], Jaime Espino [1], Pascual Bartolo-Pérez [2], Geonel Rodríguez-Gattorno [2] and Juan José Alvarado-Gil [2]

1 División de estudios de Posgrado, Facultad de Ingeniería Química, Universidad Michoacana de S.N.H. Morelia Z.P. 58060, Michoacán, Mexico; cedegarci@gmail.com (V.J.C.); jespinova@yahoo.com.mx (J.E.)
2 CINVESTAV-IPN, Unidad Mérida. Mérida Z.P.97310, Yucatán, Mexico; pascual@cinvestav.mx (P.B.-P.); geonelr@gmail.com (G.R.-G.); jjag09g@gmail.com (J.J.A.-G.)
* Correspondence: rrangel@umich.mx; Tel.: +52-443-327-3584

Received: 27 November 2018; Accepted: 13 December 2018; Published: 19 December 2018

Abstract: In this study, we tested the efficiency of nitrogen-doped titanium dioxide (N-TiO_2) and nitrogen-doped bismuth molybdate (N-Bi_2MoO_6) compounds as photocatalysts capable of degrading methylene blue and lignin molecules under irradiation with ultraviolet (UV) and visible light (VIS). Moreover, we compared TiO_2 and Bi_2MoO_6 catalysts with N-TiO_2 and N-Bi_2MoO_6 compounds using chemical coprecipitation. The catalysts were prepared starting from $Ti(OCH_2CH_2CH_3)_4$, $Bi(NO_3)_3{\cdot}5H_2O$, and $(NH_4)_6Mo_7O_{24}$ reagents. N-doping was achieved in a continuous reflux system, using ethylene diamine as a nitrogen source. The resulting materials were characterized using Scanning Electron Microscopy (SEM), X-Ray diffraction (XRD), Fourier transform infrared spectroscopy (FTIR), and X-ray photoelectron spectroscopy (XPS). Additionally, we observed the decrease in particle size after processing the compounds in the reflux system. The results regarding photocatalytic degradation tests show a remarkable effect for nitrogen doped samples, achieving 90% of lignin degradation.

Keywords: photocatalysis; Titanium dioxide; bismuth molybdate; lignin; UV light; visible light

1. Introduction

Advanced oxidation processes (AOP) are commonly seen as an alternative to degraded environmental water pollutants, based on their effectiveness, high reactivity, non-selectivity, and their extensive variety of applications [1]. Since its inception [2], titanium oxide remains one of the most effective and versatile compounds for photocatalytic applications, even if traditional compounds like ZnO [3], CdS [4], SnO_2 [5], ZnS [6], and $BiVO_4$ [7] have been tested to improve their efficiency or performance in comparison to TiO_2. Another aspect commonly used to enhance photocatalytic yield is the process manipulation that produces different structural features of TiO_2 particles, such as specific surface area or shape. Some of these manipulations include chemical coprecipitation [8], sol-gel combustion method [9], spray drying [10], or microwave heating [11]. Most of those studies were used to reduce or control the crystal size and had the purpose of increasing the volume/length ratio to maximize the exposed surface, thus increasing the active sites to achieve the catalytic process more effectively, in terms of reactivity [12]. In the majority of reported studies, the results are marginal in comparison to TiO_2. Only few compounds, including ZnO or Bi_2MoO_6, have exhibited promising results in enhancing the catalytic activity in at least one order of magnitude [13,14]. ZnO is as a robust candidate for wastewater treatment, due to its similarity with TiO_2, in aspects such as

charge carrier dynamics upon bandgap excitation and the generation of reactive oxygen species in aqueous suspensions. However, inherent details like its wide band gap and massive charge carrier recombination has limited their massive usage [3].

Bismuth molybdate (Bi_2MoO_6) has been profusely studied in the past as a catalyst in oxidation reactions [15]. At the present time, Bi_2MoO_6 has attracted a lot of attention in photocatalysis research, due to their effectiveness to degrade organic pollutants under UV irradiation. The Bi_2MoO_6 morphology [16,17] and production methods include sol-gel [18], solvothermal synthesis [19], and co-precipitation [20], among others.

An alternative method to increase the catalytic activity of some photocatalytic materials is through the inclusion of some relevant dopant elements, either by using transition metal cations to replace metal sites [21] or by inserting nonmetal anions like F [22], C [23], or N [24].

The purpose is to create new electronic states between the valence and conduction bands, facilitating the electron conduction to enhance the photocatalytic efficiency and also favoring the electron-hole formation. In addition, those new states promote the shifting towards the visible region of the electromagnetic spectrum. In this regard, nitrogen-doping has been considered one of most effective approaches to improve photocatalytic activity of TiO_2 in the visible region [25]. The methods currently reported to achieve it superficially or by replacing atoms include ion implantation [26], physical vapor deposition [27], and spray pyrolysis [28], as well as variants of the known process of sol-gel. An alternative method to include nitrogen is the refluxing methodology, which consists of inducing intimate contact between the nitrogen source precursor (hydrazine, urea, ethylene diamine, etc.) and the catalyst inside a closed system of reflux at constant temperature. As a result of that methodology, it is possible to obtain catalysts containing nitrogen [29]. The amount of nitrogen that can be introduced depends on factors including the type of precursor, the reflux temperature, and the time involved.

The purpose of the present research was to study the efficiency of titanium oxide and bismuth molybdate, both nitrogen-doped, to be tested as photocatalysts capable of degrading the methylene blue (MB) dye, which is considered as a model molecule for degradation studies.

Additionally, we studied the photodegradation of lignin using both kinds of compounds. Lignin is a compound commonly found in wastewater from the wood process manufacturing. Usually, lignin is partially solubilized with acid and their product is concentrated and burned. Even so, some residual amount of lignin remains bonded to cellulose, which in many cases, is discarded to body waters affecting the environment and altering the photosynthetic processes. Our hypothesis is that nitrogen doping on TiO_2 and Bi_2MoO_6 will make the photocatalytic oxidation process more efficient, this achieving the lignin degradation.

2. Results

2.1. Scanning Electron Microscopy (SEM)

The morphology of samples was analyzed using Scanning Electron Microscopy (SEM). The Figure 1a displays a SEM image of TiO_2, which shows spherical and defined morphology. The N-doped TiO_2 compound, presented in Figure 1b, shows agglomerates of nano particles in a range of 0.1 to 0.5 µm. The image 1c of Bi_2MoO_6 displays laminar particles of an N-doped Bi_2MoO_6 compound. Figure 1d exhibits defined, elongated bar-like shaped particles with smooth edges.

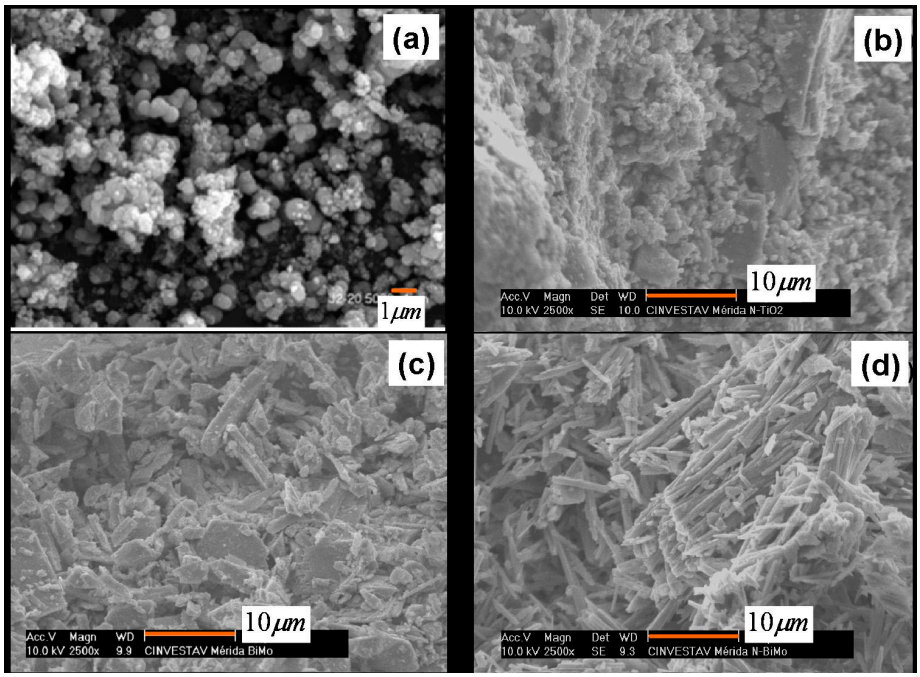

Figure 1. Scanning Electron Microscopy (SEM) photo-micrograph obtained at 5000X of (**a**) titanium dioxide (TiO_2), (**b**) nitrogen-doped titanium dioxide (N-TiO_2), (**c**) bismuth molybdate (Bi_2MoO_6), and (**d**) nitrogen-doped bismuth molybdate (N-Bi_2MoO_6) Bi_2MoO_6 catalysts.

2.2. X-ray Diffraction Analysis

X-ray analyses were carried out in order to capture pristine TiO_2 and Bi_2MoO_6 catalysts. I addition, they were carried out for their corresponding nitrogen doped compounds. For TiO_2 compounds, X-ray diffraction (XRD) patterns are displayed in Figure 2. It can be observed that this sample matches well with the anatase phase reported for TiO_2. For the N-doped TiO_2 sample, wider peaks are observed, as are changes in the intensity of the (101) diffraction plane, revealing that after N-doping through the reflux system, TiO_2 particles become smaller in size, providing the characteristic spectrum of an amorphous material. Figure 3 shows the diffraction pattern for Bi_2MoO_6 compounds, which reveals how the orthorhombic phase, also known as γ-Bi_2MoO_6 phase, was stabilized in these compounds. The crystallite size was calculated for every system using the Scherrer equation, which is as follows:

$$L = \frac{k\lambda}{W cos\Theta} \quad (1)$$

where k is a constant that depends on particle morphology (usually k = 1.0 for cubic or nearly-cubic systems); λ is the Cu, K_α radiation (nm); W is the full width at half-maximum (rad); and Θ is the diffraction angle (deg). The (101) reflection was used to perform calculations through Equation (1) for TiO_2 compounds, while the (131) reflection was used to obtain the crystallite size for Bi_2MoO_6 compounds. The results were 8.6 nm for TiO_2, 4.01 nm for N-doped TiO_2, 16.14 nm for γ-Bi_2MoO_6. and 7.92 nm for N-doped Bi_2MoO_6. Briefly, it appeared that nitrogen doping inhibited the crystal growth.

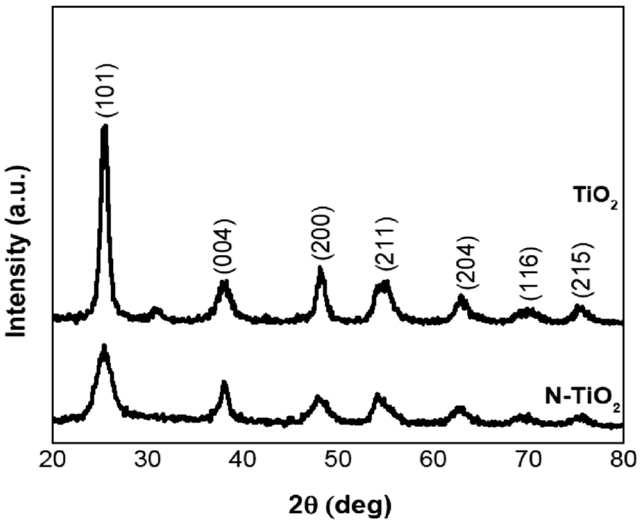

Figure 2. X-ray diffraction (XRD) patterns of TiO_2 and N-TiO_2.

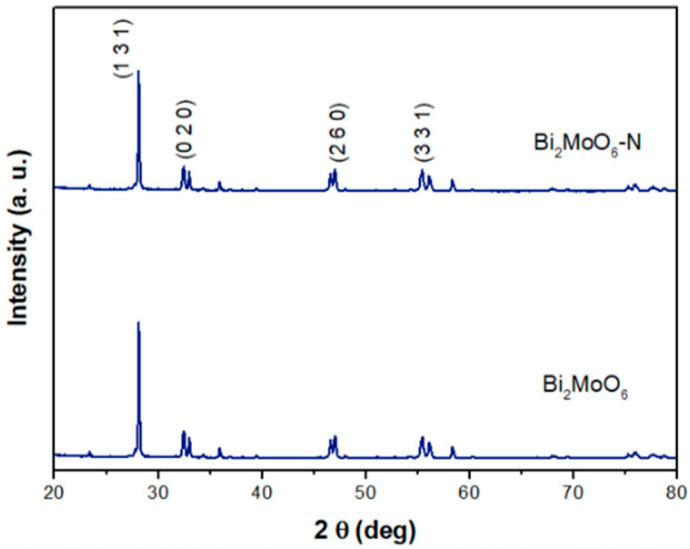

Figure 3. XRD patterns for Bi_2MoO_6 and Bi_2MoO_6-N catalysts.

2.3. Specific Surface Area Determination

The textural properties of TiO_2, Bi_2MoO_6, and N-doped catalysts are summarized in Table 1. It was appreciated that after doping TiO_2 and Bi_2MoO_6, their surface area changed in comparison to the pristine compounds. A dramatic change was observed for the TiO_2 compound which, after doping, decreased their BET area by 37%, while specific surface for Bi_2MoO_6 area was reduced to 47%. Apparently, the nitration process in both systems entails amorphization and pore reduction.

Table 1. Specific surface area for TiO_2, Bi_2MoO_6, TiO_2-N, and Bi_2MoO_6-N catalysts.

Compound	BET Surface Area (m^2/g)
TiO_2	117.0
N-TiO_2	73.7
Bi_2MoO_6	3.8
N-Bi_2MoO_6	2.0

Through the reflux procedure, carried out for at least 2 h, the constant movement of the particles in intimate contact with the ethylene-diamine and 1-hexanol resulted in a separation of the initially

obtained particles, modifying the size of aggregates towards smaller values, which impacted the specific surface area. The resulting particles were smaller on average, especially in comparison to pristine undoped TiO_2 or Bi_2MoO_6 compounds, in the order of nanometers. While this process occurred, nitrogen molecules were fixed on the surface blocking pores and contributed to an apparent decrease in the specific surface area.

2.4. Diffuse Reflectance Measurements

Because the use of visible energy is necessary to test these systems, it is important to determine if there are any energy gap reductions after conducting the doping process. Thus, the diffuse reflectance spectra were obtained (Figure 4) and transformed into F(R), with a magnitude proportional to the extinction coefficient through the Kubelka-Munk function. In this case, R is the absolute reflectance of the sampled layer. Therefore, it is inferred that by using the following equation, the energy gap could be obtained graphically.

$$[F(R)h\nu]^2 = C(h\nu - Eg) \quad (2)$$

where *Eg* is the energy gap for every sample.

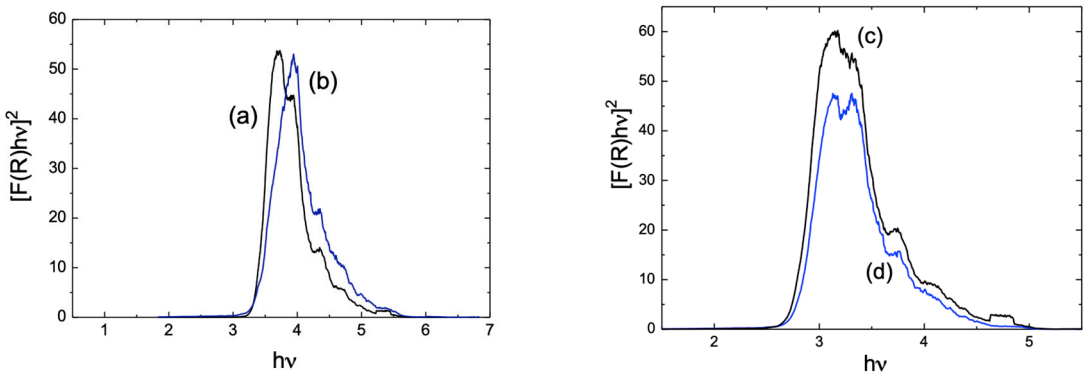

Figure 4. Reflectance diffuse measurements for (**a**) N-TiO_2, (**b**) TiO_2, (**c**) N-Bi_2MoO_6, and (**d**) Bi_2MoO_6, compounds.

The values obtained for the band gap are summarized in Table 2, where it is appreciated that, in both cases, a decreasing occurs after the nitrogen doping. These results indicate the possibility of using the developed compounds as a photocatalyst in the visible region of the electromagnetic spectrum, which will be demonstrated later in this work.

Table 2. Gap values for TiO_2, Bi_2MoO_6, N-TiO_2, and N-Bi_2MoO_6 catalysts.

Compound	Experimental Gap, eV	Reported Gap, eV
TiO_2	3.17	3.20
N-TiO_2	2.96	
Bi_2MoO_6	2.84	2.90
N-Bi_2MoO_6	2.73	

2.5. X-ray Photoelectron Spectroscopy (XPS)

XPS analyses were performed in samples with the purpose of establishing present elements and especially to determine if nitrogen doping is detected in TiO_2 or Bi_2MoO_6 doped compounds. Figure 5 shows the XPS spectra for TiO_2 and TiO_2-N compounds. The lower image, in this figure, corresponds to the pristine TiO_2, where the peaks O1s and Ti 2p are pointed out, as well as the C 1s. This last peak corresponds to small traces of carbon. In the upper part of Figure 5, it can be seen the corresponding image to N-TiO_2. On it, O1s, Ti 2p which were detected, and the N 1s signal was also found. In addition, a high-resolution scanning analysis was from 390 to 410 eV was performed,

aimed at demonstrating the presence of nitrogen, which is shown as inset in the same figure. The XPS results for the Bi_2MoO_6 compounds are included in Figure 6, where the XPS spectra was acquired from 0–700 eV. The image shows the $3p_{3/2}$, 3d, and 4p states for Mo and Bi 4f, but also the O 1s and N 1 transitions are pointed out. In the upper left, an inset corresponding to the high-resolution energy window for N has been included, in order to emphasize their presence. In this way, for both cases, it is demonstrated that the procedure to introduce or impregnate nitrogen has been carried out successfully. Our results are in agreement with those results reported by other authors regarding the position of the N peak [26–28].

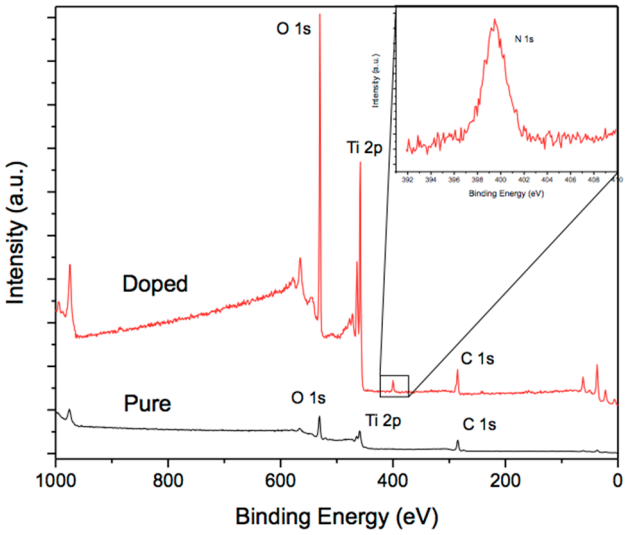

Figure 5. X-ray Photoelectron Spectroscopy (XPS) analysis for TiO_2 and N-TiO_2 catalysts.

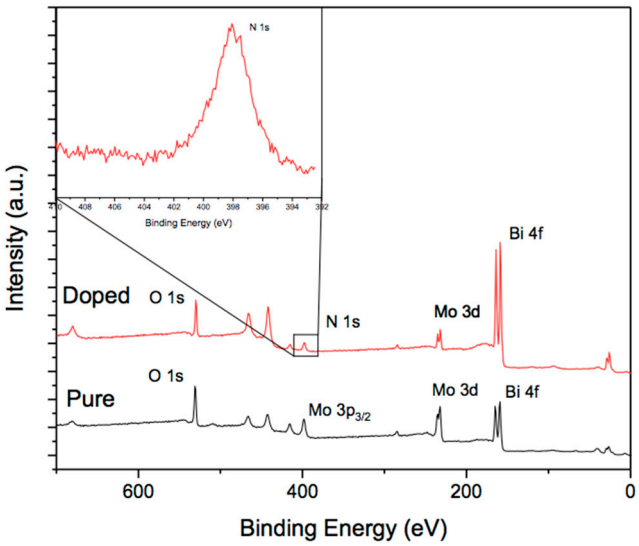

Figure 6. XPS analysis for Bi_2MoO_6 and N-Bi_2MoO_6 catalysts.

The quantification of the elements through the integration under the curve of each of their corresponding reflections gave us the following values summarized in Table 3.

It is observed that titanium oxide compounds are closer to the TiO_2 stoichiometry in comparison to Bi_2MoO_6 compounds. The reason is that usually bismuth tends to segregate close to the surface in the calcination stage, altering in some proportion the desired stoichiometry, as has been discussed in previous works [19,20]. It is important to note that the nitrogen content for N-Bi_2MoO_6 is larger than the value obtained for N-TiO_2. However, it will be shown in the next section that N-TiO_2 exhibits

better performance in terms of catalytic activity. This means that the proportion of nitrogen has specific effects for every compound, as will be demonstrated latter.

Table 3. Atomic percent values from XPS analyses for TiO_2, Bi_2MoO_6, N-TiO_2, and N-Bi_2MoO_6 catalysts.

Compound	Ti2p	O1s	N1s	Bi	Mo
TiO_2	22.73	67.77	-	-	-
N-TiO_2	27.01	67.05	5.94	-	-
Bi_2MoO_6	-	61.86	-	24.12	14.02
N-Bi_2MoO_6	-	52.3	13.38	25.29	9.04

3. Photocatalytic Activity Tests

Figures 7–9 show photocatalytic activity measurements and solutions containing TiO_2 or Bi_2MoO_6 compounds. The reaction under ultraviolet (UV) and visible light (VIS) was evaluated separately for both, specifically methylene blue and lignin samples, which were measured to have an optical absorption at 660 nm and 289 nm, respectively. Pristine TiO_2 or Bi_2MoO_6 compounds were tested for MB degradation for about 120 min in the UV range (Figure 7). The degradation reached for TiO_2 was 80%, while for Bi_2MoO_6 it was nearly 70%. On the other hand, both compounds showed an improved degradation behavior when doped with nitrogen, reaching 90% of MB degradation using N-Bi_2MoO_6 and 93% for N-TiO_2. After the MB tests, both Bi_2MoO_6 and TiO_2 compounds were studied for lignin degradation, which is a more complex organic structure, when compared to MB. The degradation attained for Bi_2MoO_6 was about 62%; the degradation attained for TiO_2 was about 70% (Figure 8). In the case of nitrogen-doped compounds, the degradation was 82% for Bi_2MoO_6–N and 93% for N-TiO_2. Figure 8 summarizes the results obtained for lignin degradation that used TiO_2, N-TiO_2, Bi_2MoO_6, and N-Bi_2MoO_6 catalysts under visible light. Regarding the TiO_2 compound, it was less sensitive to VIS irradiation in such a way that only 12% degradation for TiO_2 and 25% for Bi_2MoO_6 were found. These results reveal the complex nature of the lignin molecule, which is hard to degrade and frequently results in compounds derived from this degradation, such as formic acid, ketones, and aldehydes, among others [30–33]. An interesting result was found for lignin degradation when using N-TiO_2 and N-Bi_2MoO_6 catalysts (Figure 9), where a 32% degradation for N-TiO_2 catalyst and 38% for N-Bi_2MoO_6 compound can be observed. Interestingly, nitrogen doping on both compounds, has been beneficial. However, the nitrogen doping in TiO_2 makes this material more efficient, which can be related to the reduction of the energy gap, which would be able to provide additional electronic states among conduction and valence bands.

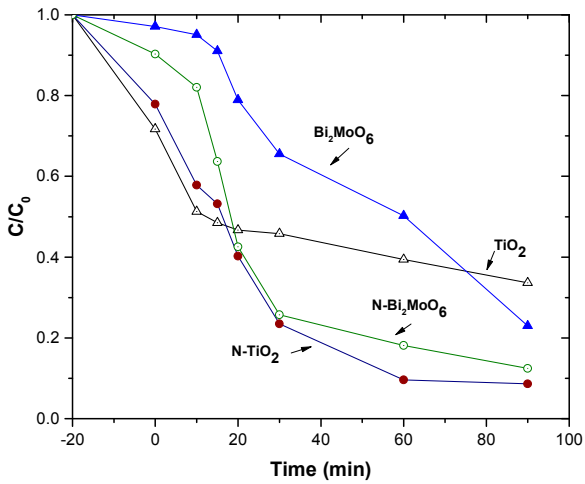

Figure 7. Methylene blue degradation in presence of TiO_2, N-TiO_2, Bi_2MoO_6, and N-Bi_2MoO_6 catalysts under visible light (VIS) energy irradiation.

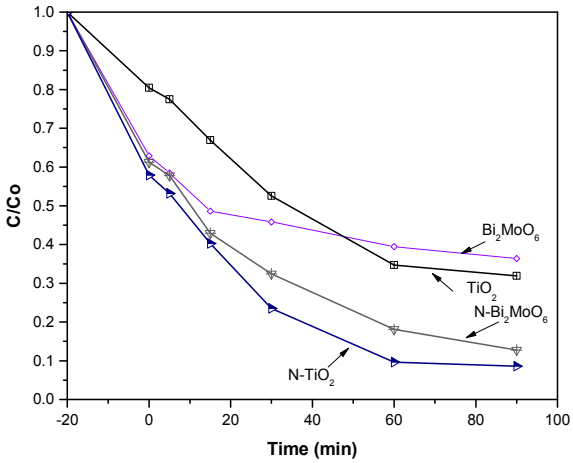

Figure 8. Lignin degradation in presence of TiO_2, N-TiO_2, Bi_2MoO_6, and N-Bi_2MoO_6 catalysts under ultraviolet (UV) energy irradiation.

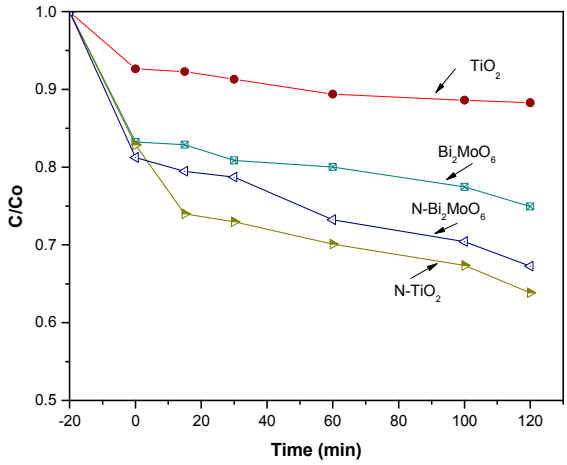

Figure 9. Lignin degradation in presence of TiO_2, N-TiO_2, Bi_2MoO_6, and N-Bi_2MoO_6 catalysts under VIS energy irradiation.

4. Methods and Materials

4.1. Synthesis of TiO_2 and Bi_2MoO_6 Catalysts

A TiO_2 material was based on colloidal TiO_2 obtained from $Ti[OCH(CH_3)_2]_4$ hydrolysis and stirring the suspension to obtain the gel. The resulting material was filtered and oven dried at 100 °C and finally calcined at 450 °C. The Bi_2MoO_6 compound was obtained using chemical coprecipitation starting with high purity $Bi(NO_3)_3{\cdot}5H_2O$ and $(NH_4)_6Mo_7O_{24}$, diluted in distilled water and adjusting the pH 7.0 using either NH_4OH or HNO_3. Afterward, the precipitated Bi_2MoO_6 was washed and oven-dried at 100 °C and calcined at 400 °C.

4.2. Synthesis of N-doped TiO_2 and N-doped Bi_2MoO_6

In order to obtain N-doped Bi_2MoO_6 and N-doped TiO_2 catalysts, both compounds separately, were added with 25 mL of a 2 M ethylene diamine solution and 150 mL of 1-hexanol, in a continuous refluxing system, stirring it for 2 h. Afterward, N-doped Bi_2MoO_6 and N-doped TiO_2 materials were filtered, washed several times with water, and dried in an oven at 200 °C. Upon drying, both compounds yielded an intense yellowish powder.

4.3. Characterization Details

The obtained compounds were characterized using X-ray diffraction (Siemens, D-5000 model), operating at 30 keV and 20 mA, with a step size 0.02°/min from 10 to 70°(2θ). The images were obtained in a SEM JSM-6400 JEOL Noran Instruments, at 20 keV and 10^{-6} Torr. The diffuse reflectance spectra (R) data were obtained using a UV-visible spectrophotometer (AvaSpec-2048), equipped with an integrating sphere (Ocean Optics, Mod. ISP-50-8-R-GT), equipped with a deuterium halogen light source (Mod. AvaLight DH-S-BAL). Specific surface area was measured in a Micrometrics Gemini 2060 RIG-100, model at 77 K using the BET method. For the XPS analyses, samples were excited with Al and Ka X-rays with an energy of 1486.6 eV. The spectrometer was calibrated using the Cu 2p3/2 (932.4 eV) and Cu 3p3/2 (74.9 eV) lines. Binding energy calibration was based on C 1s at 284.6 eV.

4.4. Photocatalytic Evaluation

Catalytic activity was tested as previously described [30,31]. Briefly, the reaction was carried out in a batch micro reactor provided with an oxygen flow, to generate superoxide radicals and prevent electron recombination. The solution was previously stirred for 20 min without the presence of light in order to reach a stable MB or lignin absorbance on the photocatalyst surface. Then, the solution was irradiated with the source of light, magnetically stirred, and air was introduced once the reaction system was started. For MB studies, 0.1 g of every catalyst were placed into a beaker containing an aqueous solution of 0.2 g/L of MB. Regarding the lignin degradation, 0.2 g of this compound (Sigma-Aldrich, PM = 28,000 g/mol) was mixed with 15 mL of NaOH (Sigma-Aldrich, México city, México); 0.05 M was used to dissolve the samples, where then the samples were placed into a beaker containing 500 mL of deionized water. The pH = 8 was adjusted to enhance the photo catalytic reaction, according to reference [32]. For every catalyst, the reaction was achieved for 80 min. Samples were taken from the reactor system at 20 min intervals to follow the course of the reaction. Samples were centrifuged for 5 min at 220 rpm, in order to separate the catalyst from the solution to determine the progress of the reaction. A UV light lamp was used with a wavelength of 365 nm for the photocatalytic reaction. In the case of the visible light experiments, the irradiation was performed using a UV-VIS light source of 200 W, provided with a Xe arc lamp (Oriel). The concentration was monitored through a UV-VIS Hach Dr/4000u spectrophotometer at a wavelength of 289 nm for lignin and 660 nm for MB.

5. Discussion

After the refluxing process, the dissolution and recrystallization processes of a dispersed solid under reflux (nitrogen doping) was expected. It was substantiated by the well-known Ostwald's ripening. Often, the Ostwald's ripening includes the large crystals growing at the cost of smaller ones (i.e., coarsening). In the present case, the presence of the amine might have changed the expected growth by favoring the nucleation of new parties as part of the recrystallizing processes. According to Classical Nucleation Theory (CNT), a phase transition (i.e., the crystallization of a new phase within another) can be rationalized as result of two main opposed contributions. On one hand, the driving force for the process is universally identified in chemical reactions with the chemical potential difference ($\Delta\mu$); on the other hand, the work spent to form the new surface was related to the new phase (associated with the interface energy, σ, and the area created, A) [34]. Hence, the Gibbs free energy for homogeneous nucleation was, $\Delta G = \Delta\mu + A\sigma$, where spontaneous nucleation will depend on the balance between both energies' contribution. In a heterogeneous nucleation, a surface area already exists and acts as nucleation site with lower contribution from the second term. Therefore, $\Delta G_{\text{heterogeneous}}$ becomes a fraction of $\Delta G_{\text{homogeneous}}$ [35]. This explains the well-known "coarsening" phenomena. However, the coarsening should compete with nucleation of new particles, as the amine acts as a surfactant and also decreases the second term by lowering the interfacial energy. Therefore, diminishing the particle size is intuitively expected under present conditions.

Furthermore, we cannot discard a possible amorphization process as result of the nitrogen inclusions within the matrix of the solids. Recrystallization accompanied nitrogen impurification might cause displacements of Wyckoff positions expected for the spatial groups of both solids; this could occur with the consequent strain increase that would change the Full wide half maximum (FWHM) of the reflections.

The XPS analyses have demonstrated the incorporation of nitrogen in both N-TiO_2 and N-Bi_2MoO_6 compounds. The nitrogen signal is located close to 400 eV. However, it is worth mentioning that some differences arise when this peak is closely analyzed for every compound. In the case of nitrogen doping for the TiO_2 compound, one peak is located at 397.3 eV and another in 400.7 eV. The first is attributed to substitutional or interstitial impurities (corresponding to Ti-N bonds that substitute O by N in the lattice); the other transition, located in 400.7 eV, can be attributed to molecularly chemisorbed (superficial) nitrogen. Regarding the Bi_2MoO_6 catalyst, something similar occurs when the high-resolution peak that corresponds to nitrogen is analyzed, as the peak found at 396 eV corresponds to shallow surface nitrogen, while the nitrogen signal at 398 eV can be assigned to interstitial nitrogen. In general, nitrogen doping has been beneficial in most cases, because the nitrogen doped samples showed the best degradation performance in comparison to the pristine Bi_2MoO_6 or TiO_2 catalysts. As expected, lignin degradation was more difficult to carry out in comparison to MB, due to the complexity of the lignin molecule. However, the N-TiO_2 sample showed a 90% degradation for lignin when using UV radiation. In the case of experiments carried out using visible radiation, it was found that by using an N-Bi_2MoO_6 compound, 30% degradation was attained; in the case of N-TiO_2, however, a 35% of lignin degradation was reached.

6. Conclusions

TiO_2 and Bi_2MoO_6 N-doped photocatalysts were successfully synthesized and our XPS analyses demonstrate that nitrogen doping was carried out efficiently. It was also found that the N-TiO_2 catalyst exhibited a better performance in terms of MB or lignin degradation. Even if N-TiO_2 and N-Bi_2MoO_6 catalysts provide good efficiency for MB and lignin degradation, nitrogen doped TiO_2 is the best catalyst to degrade lignin. It is demonstrated that nitrogen doping in both compounds, is an effective way to improve their degradation performance. It was also shown that nitrogen doping provides the possibility of using both catalysts under visible light.

Author Contributions: Conceptualization, R.R.; methodology, V.C.; formal analysis, P.B.; investigation, V.C.; resources, J.E.; data curation, J.E.; writing—original draft preparation, R.R.; writing—review and editing, G.R.; and J.A.

Funding: This research received no external funding.

Acknowledgments: R. Rangel acknowledges financial support from CIC-UMSNH under project 2018. Also thanks to W. Cahuich from Cinvestav-IPN for SEM images. Also to LANBIO of Cinvestav, Merida for allowing acces to their facilities.

Conflicts of Interest: The authors declare not having conflict of interest.

References

1. Fernández, C.; Larrechi, M.S.; Callao, M.P. An analytical over-view of processes for removing organic dyes from wastewater effluents. *Trends Anal. Chem.* **2010**, *29*, 1202–1211. [CrossRef]
2. Fujishima, A.; Honda, K. Electrochemical photolysis of water at a semiconductor electrode. *Nature* **1972**, *238*, 37–38. [CrossRef] [PubMed]
3. Kumar, G.; Rao, K.S.R.K. Zinc oxide based photocatalysis: Tailoring Surface–Bulk structure and related interfacial charge carrier dynamics for better environmental applications. *RSC Adv.* **2015**, *5*, 3306–3351. [CrossRef]
4. Huang, Y.; Sun, F.; Wu, T.; Wu, Q.; Huang, Z.; Su, H.; Zhang, Z. Photochemical preparation of CdS hollow microspheres at room temperature and their use in visible-light photocatalysis. *J. Solid State Chem.* **2011**, *184*, 644–648. [CrossRef]

5. Abdelkadera, E.; Nadjia, L.; Naceur, B.; Noureddine, B. SnO_2 foam grain-shaped nanoparticles: Synthesis, characterization and UVA light induced photocatalysis. *J. Alloys Compd.* **2016**, *679*, 408–419. [CrossRef]
6. Ye, Z.; Kong, L.; Chen, F.; Chen, Z.; Lin, Y.; Liu, C. A comparative study of photocatalytic activity of ZnS photocatalyst for degradation of various dyes. *Optik* **2018**, *164*, 345–354. [CrossRef]
7. Ullaha, S.; Ferreira-Neto, E.P.; Hazra, C.; Parveen, R.; Rojas-Mantilla, H.D.; Calegaro, M.L.; Serge-Correales, Y.E.; Rodrigues-Filho, U.P.; Ribeiro, S.J.L. Broad spectrum photocatalytic system based on $BiVO_4$ and $NaYbF_4$:Tm^{3+} upconversion particles for environmental remediation under UV-vis-NIR illumination. *Appl. Catal. B Environ.* **2019**, *243*, 121–135. [CrossRef]
8. Sanchez-Martinez, A.; Ceballos-Sanchez, O.; Koop-Santa, C.; López-Mena, E.R.; Orozco-Guareño, E.; García-Guaderrama, M. N-doped TiO_2 nanoparticles obtained by a facile coprecipitation method at low temperature. *Ceram. Int.* **2018**, *44*, 5273–5283. [CrossRef]
9. Moustakas, N.G.; Kontos, A.G.; Likodimos, V.; Katsaros, F.; Boukos, N.; Tsoutsou, D.; Dimoulas, A.; Romanos, G.E.; Dionysiou, D.D.; Falaras, P. Inorganic-organic core-shell titania nanoparticles for efficient visible light activated photocatalysis. *Appl. Catal. B Environ.* **2013**, *130–131*, 14–24. [CrossRef]
10. Khan, H.; Rigamonti, M.G.; Patience, G.S.; Boffito, D.C. Spray dried TiO_2/WO_3 heterostructure for photocatalytic applications with residual activity in the dark. *Appl. Catal. B Environ.* **2018**, *226*, 311–323. [CrossRef]
11. Nunes, D.; Pimentel, A.; Pinto, J.V.; Calmeiro, T.R.; Nandy, S.; Barquinha, P.; Pereira, L.; Carvalho, P.A.; Fortunato, E.; Martins, R. Photocatalytic behavior of TiO_2 films synthesized by microwave irradiation. *Cat. Today* **2016**, *278*, 262–270. [CrossRef]
12. Ramakrishnan, V.M.; Natarajan, M.; Santhanam, A.; Asokan, V.; Velauthapillai, D. Size controlled synthesis of TiO_2 nanoparticles by modified solvothermal method towards effective photo catalytic and photovoltaic applications. *Mater. Res. Bull.* **2018**, *97*, 351–360. [CrossRef]
13. Rangel, R.; Cedeño, V.; Ramos-Corona, A.; Gutierrez, R.; Alvarado-Gil, J.J.; Ares, O.; Bartolo-Perez, P.; Quintana, P. Tailoring surface and photocatalytic properties of ZnO and nitrogen-doped ZnO nanostructures using microwave-assisted facile hydrothermal synthesis. *Appl. Phys.* **2017**, *123*, 552. [CrossRef]
14. Phuruangrat, A.; Dumrongrojthanath, P.; Thongtem, S.; Thongtem, T. Synthesis and characterization of visible light-driven W-doped Bi_2MoO_6 photocatalyst and its photocatalytic activities. *Mater. Lett.* **2017**, *194*, 114–117. [CrossRef]
15. Rangel, R.; Maya, R.; García, R. Novel [$Ce_{1-X}La_xO_2$, $La_{2-y}Ce_yO_3$]/$Bi_2Mo_{0.9}W_{0.1}O_6$ Catalysts for CO Oxidation at low temperature. *Catal. Sci. Technol.* **2012**, *2*, 639–642. [CrossRef]
16. Geng, B.; Wei, B.; Gao, H.; Xu, L. Ag_2O nanoparticles decorated hierarchical Bi_2MoO_6 microspheres for efficient visible light photocatalysts. *J. Alloys Compd.* **2017**, *699*, 783–787. [CrossRef]
17. Guo, J.; Shi, L.; Zhao, J.; Wang, Y.; Yuan, X. Enhanced visible-light photocatalytic activity of Bi2MoO6 nanoplates with heterogeneous $Bi_2MoO_{6\text{-}x}$ and Bi_2MoO_6 core-shell structure. *App. Catal. B Environ.* **2018**, *224*, 692–704. [CrossRef]
18. Umapathy, V.; Manikandan, A.; Antony, S.A.; Ramu, P.; Neeraja, P. Structure, morphology and opto-magnetic properties of Bi_2MoO_6 nano-photocatalyst synthesized by sol-gel method. *Trans. Nonferrous Metals Soc. China* **2015**, *25*, 3271–3278. [CrossRef]
19. Bi, J.; Wu, L.; Li, J.; Li, Z.; Wang, X.; Fu, X. Simple solvothermal routes to synthesize nanocrystalline Bi_2MoO_6 photocatalysts with different morphologies. *Acta Mater.* **2007**, *55*, 4699–4705. [CrossRef]
20. Martínez-de la Cruz, A.; Obregón Alfaro, S. Synthesis and characterization of γ-Bi_2MoO_6 prepared by co-precipitation: Photoassisted degradation of organic dyes under vis-irradiation. *J. Mol. Catal. A Chem.* **2010**, *320*, 85–91. [CrossRef]
21. Jin, S.; Hao, H.; Gan, Y.; Guo, W.; Li, H.; Hu, X.; Hou, H.; Zhang, G.; Yan, S.; Gao, W.; et al. Preparation and improved photocatalytic activities of Ho^{3+}/Yb^{3+} co-doped Bi_2MoO_6. *Mater. Chem. Phys.* **2017**, *199*, 107–112. [CrossRef]
22. Yu, Ch.; Wu, Z.; Liu, R.; Dionysiou, D.D.; Yang, K.; Wang, Ch.; Liu, H. Novel fluorinated Bi_2MoO_6 nanocrystals for efficient photocatalytic removal of water organic pollutants under different light source illumination. *App. Catal. B Environ.* **2017**, *209*, 1–11. [CrossRef]
23. Xing, Y.; Gao, X.; Ji, G.; Liu, Z.; Du, C. Synthesis of carbon doped Bi_2MoO_6 for enhanced photocatalytic performance and tumor photodynamic therapy efficiency. *Appl. Surf. Sci.* **2019**, *465*, 369–382. [CrossRef]

24. Asashi, R.; Morikawa, T.; Ohwaki, T.; Aoki, K.; Taga, Y. Visible light photocatalysis in nitrogen-doped titanium oxide. *Science* **2001**, *293*, 269–271. [CrossRef] [PubMed]
25. Wang, J.; Tafen, D.; Lewis, J.; Hong, Z.; Manivannan, A.; Zhi, M.; Wu, N. Origin of photocatalytic activity of nitrogen-doped TiO_2 nanobelts. *J. Am. Chem. Soc.* **2009**, *131*, 12290–12297. [CrossRef] [PubMed]
26. Yoshida, T.; Niimi, S.; Yamamoto, M.; Ogawa, S.; Nomoto, T.; Yagi, S. Characterization of nitrogen ion implanted TiO_2 photocatalysts by XAFS and XPS. *Nucl. Instrum. Methods Phys. Res. Sect. B: Beam Interact. Mater. At.* **2015**, *365*, 79–81. [CrossRef]
27. Manova, D.; Franco-Arias, L.; Hofele, A.; Alani, I.; Kleiman, A.; Asenova, I.; Decker, U.; Marquez, A.; Mändl, S. Nitrogen incorporation during PVD deposition of TiO_2:N thin films. *Surf. Coat. Technol.* **2017**, *312*, 61–65. [CrossRef]
28. Boningaria, T.; Reddy-Inturia, S.N.; Suidan, D.; Smirniotisa, P.G. Novel one-step synthesis of nitrogen-doped TiO_2 by flame aerosol technique T for visible-light photocatalysis: Effect of synthesis parameters and secondary nitrogen (N) source. *Chem. Eng. J.* **2018**, *350*, 324–334. [CrossRef]
29. Tran, V.A.; Truong, T.T.; Pham-Phan, T.A.; Nguyen, T.N.; Huynh, T.V.; Agresti, A.; Pescetelli, S.; Le, T.K.; Carlo, A.; Lund, T.; et al. Application of nitrogen-doped TiO_2 nano-tubes in dye-sensitized solar cells. *Appl. Surf. Sci.* **2017**, *399*, 515–522. [CrossRef]
30. Rangel, R.; López-Mercado, G.J.; Bartolo-Pérez, P.; García, R. Nanostructured-[CeO_2, La_2O_3, C]/TiO_2 catalysts for lignin photodegradation. *Sci. Adv. Mater.* **2012**, *4*, 573–578. [CrossRef]
31. Rangel, R.; García-Espinoza, J.D.; Espitia-Cabrera, I.; Alvarado-Gil, J.J.; Quintana, P.; Bartolo-Pérez, P.; Trejo-Tzab, R. Synthesis of Mesoporous of $N_yTi_{1-x}Ce_xO_{2-y}$ Structures and its Visible Light Induced Photocatalytic Performance. *Nano* **2013**, *8*, 1350051–1350061. [CrossRef]
32. Dahm, A.; Lucian, A. Titanium dioxide catalyzed photodegradation of lignin in industrial effluents. *Ind. Eng. Chem. Res.* **2004**, *43*, 7996–8000. [CrossRef]
33. Gazi, S.; Hung Ng, W.K.; Ganguly, R.; Putra, A.M.; Hirao, H.; Soo, H.S. Selective photocatalytic C–C bond cleavage under ambient conditions with earth abundant vanadium complexes. *Chem. Sci.* **2015**, *6*, 7130–7142. [CrossRef] [PubMed]
34. La Mer, V.K; Dinegar, R.H. Theory, Production and Mechanism of Formation of Monodispersed Hydrosols. *Ind. Eng. Chem.* **1950**, *72*, 4847–4854.
35. Wnek, W.J. The simulation of precipitation kinetics. *Powder Technol.* **1978**, *20*, 289–293. [CrossRef]